Monthly Notices
of the
ROYAL ASTRONOMICAL SOCIETY

MNRAS **470,** 1703–1717 (2017)
Advance Access publication 2017 May 29

doi:10.1093/mnras/stx1322

Integral field spectroscopy of the inner kpc of the elliptical galaxy NGC 5044

Suzi I. F. Diniz,[1⋆] Miriani G. Pastoriza,[1⋆] Jose A. Hernandez-Jimenez,[1,3] Rogerio Riffel,[1⋆] Tiago V. Ricci,[2] João E. Steiner[3] and Rogemar A. Riffel[4]

[1]*Instituto de Física, Universidade Federal do Rio Grande do Sul, CP 15051, 91501-970 Porto Alegre, RS, Brazil*
[2]*Universidade Federal da Fronteira Sul, Campus Cerro Largo, Rua Major Antonio Cardoso, Cerro Largo, RS 97900-000, Brazil*
[3]*Instituto de Astronomia, Geofísica e Ciências Atmosféricas, Universidade de São Paulo, 05508-900 São Paulo, Brazil*
[4]*Departamento de Física, Centro de Ciências Naturais e Exatas, Universidade Federal de Santa Maria, 97105-900 Santa Maria, RS, Brazil*

Accepted 2017 May 24. Received 2017 May 24; in original form 2016 July 19

ABSTRACT

We used Gemini Multi-Object Spectrograph in the integral field unit mode to map the stellar population, emission-line flux distributions and gas kinematics in the inner kpc of NGC 5044. From the stellar populations synthesis, we found that the continuum emission is dominated by old high metallicity stars (∼13 Gyr, 2.5 $Z_{\odot}$). Also, its nuclear emission is diluted by a non-thermal emission, which we attribute to the presence of a weak active galactic nucleus (AGN). In addition, we report for the first time a broad component (FWHM ∼ 3000 km s^{-1}) in the Hα emission line in the nuclear region of NGC 5044. By using emission-line ratio diagnostic diagrams, we found that two dominant ionization processes coexist, while the nuclear region (inner 200 pc) is ionized by a low-luminosity AGN, the filamentary structures are consistent with being excited by shocks. The Hα velocity field shows evidence of a rotating disc, which has a velocity amplitude of ∼240 km s^{-1} at ∼136 pc from the nucleus. Assuming a Keplerian approach, we estimated that the mass inside this radius is 1.9×10^9 $M_{\odot}$, which is in agreement with the value obtained through the M–σ relation, $M_{\rm SMBH} = 1.8 \pm 1.6 \times 10^9$ $M_{\odot}$. Modelling the ionized gas velocity field by a rotating disc component plus inflows towards the nucleus along filamentary structures, we obtain a mass inflow rate of ∼0.4 $M_{\odot}$. This inflow rate is enough to power the central AGNs in NGC 5044.

Key words: galaxies: individual: (NGC 5044) – galaxies: kinematics and dynamics – galaxies: stellar content.

1 INTRODUCTION

It is known for a long time that many elliptical galaxies show discs, as well as filaments of ionized gas (Macchetto et al. 1996; Ferrari et al. 1999; Tran et al. 2001). Many of the early-type emission-line galaxies show characteristic spectra of a low-ionization nuclear emission-line region (LINER; Heckman 1980). However, the ionization mechanisms of this gas are still matter of debate. For example, very recently, Ricci, Steiner & Menezes (2015) studied early-type galaxies with ionized gas using optical integral field spectroscopy (IFS) and found that the Hα flux along the disc cannot be explained only by ionizing photons emitted by an active galactic nucleus (AGN). Other mechanisms, like ionization by shock (Heckman 1980; Dopita & Sutherland 1995; Allen et al. 2008; Dopita et al. 2015) or post-asymptotic giant branch (post-AGB) stars (Stasinska et al. 2008; Singh et al. 2013), can also explain the observed spectra. This may suggest that the gas is being ionized by more than one ionization mechanism.

Furthermore, large amount of molecular gas (up to 10^7 $M_{\odot}$ revelled by CO(2−1) 1.3 mm and H_2 2.121 μm emission) was found for a sample of bulge-dominated galaxies with dust lanes, revelling the complexity of these galaxies (Strong et al. 1988; David et al. 2014; Davis et al. 2015). It was suggested that this molecular and atomic gas would be accreted through a recent merger with a gas-rich galaxy and/or that it originates from a cooling flow (David et al. 2014; O'Sullivan et al. 2014). In addition, interstellar dust, mixed with the molecular and atomic gas is observed in early-type galaxies (e.g. Davis et al. 2015, and references therein). Discs and dust filaments at kpc scales (with mass between 10 and 200 $M_{\odot}$ and mid-infrared luminosity up to 14.6×10^8 $L_{\odot}$) following the ionized gas distribution were also reported in early-type galaxies (Goudfrooij et al. 1994; Ferrari et al. 1999, 2002).

Nowadays, galaxies with LINER-like spectrum are defined based on the optical line ratios (Ho 2008): [O I] λ6300/[O III] λ5007 ≥ 1/3,

⋆ E-mail: diniz.sif@gmail.com (SIFD); miriani.pastoriza@ufrgs.br (MGP); riffel@ufrgs.br (RR)

[N II] λ6583/H $\alpha \geq 0.6$, [O III] λ5007/H $\beta \leq 3$. In addition, over the last 30 yr the most accepted explanation was that these objects are powered by weak AGNs (Ferland & Netzer 1983; Halpern & Steiner 1983). However, in the last few years contradictory results were found between the AGN-ionization scenario and predicted emission-line strengths (Cid Fernandes et al. 2011) or with the spatial distribution of the ionized gas regions (e.g. Sarzi et al. 2010; Yan & Blanton 2012; Martins et al. 2013; Belfiore et al. 2015). In addition, using the Calar Alto Legacy Integral Field Area (CALIFA; Sánchez et al. 2012) survey of spatially resolved data, Singh et al. (2013) have shown that galaxies with LINER-like spectrum are powered by hot old stars and accreting black holes are rare. In this work, we propose to test this hypothesis by mapping in details the emission gas and stellar populations in the inner kiloparsec in a key object – the gas-rich early-type galaxy NGC 5044.

NGC 5044 was observed over almost the entire electromagnetic spectrum, presenting rich structures, such as gas and dust filaments (Ferrari et al. 1999). It presents a very bright ionized gas emission in the form of filaments extending up to 10 kpc with a complex kinematics (Macchetto et al. 1996). Its radial velocity is blueshifted with respect to the systemic stellar velocity and the inner parts of the stellar velocity curves present counter-rotation with respect to the galaxy outer regions (Caon, Macchetto & Pastroriza 2000).

The gas ionization mechanism of NGC5044 has been the aim of several studies, for example, Rickes, Pastoriza & Bonatto (2004) suggest that the gas in the central region (∼4 arcsec) of NGC 5044 is ionized by a low-luminosity AGN (LLAGN), while the outer regions are explained by post-AGB stars (see also Macchetto et al. 1996). In addition, the overall stellar emission of this galaxy seems to be dominated by old stars over a large wavelength range, from UV (Annibali et al. 2007; Marino et al. 2011), optical (Rickes et al. 2004) and mid-infrared observations (Vega et al. 2010). Unusual polycyclic aromatic hydrocarbons (PAHs) emission was detected in *Spitzer*-IRS observations by Vega et al. (2010), this emission was not expected in this galaxy because PAH is a typical feature in star-forming galaxies. Moreover, the IRS spectrum of this object displays strong H_2 molecular and atomic gas emission (Vega et al. 2010; Panuzzo et al. 2011). Furthermore, this galaxy shows several X-ray cavities within the inner 10 kpc, which are attributed to multiple AGN outbursts over past 10^8 yr (David et al. 2009; Gastaldello et al. 2009). Moreover, David et al. (2014) using Atacama Large Millimeter/submillimeter Array (ALMA) data argue that the detection of 230 GHz continuum emission shows that it is currently going through another outburst, probably due a recent accretion event. In addition, these authors report the detection of cold molecular CO gas moving towards the centre of this galaxy, and suggested that it can be interpreted as the presence of a cooling flow in the galaxy centre direction.

We present in this paper for the first time the optical IFS obtained with Gemini Multi-Object Spectrograph (GMOS) in integral field unit (IFU) of the central 1 kpc of NGC 5044, whose gas ionization source is still controversial. Beside that, there is no information about its central gas kinematics. Although strong evidence suggests possible presence of a contribution of an AGN, other energy source also seem to be present in this galaxy ionizing their extended filaments (Macchetto et al. 1996; Rickes et al. 2004). This data allowed us to spatially resolve the inner kpc of this source and to map the possible ionization mechanisms through the analysis of stellar populations and emission-line flux ratios. The goals of this work are to establish the star formation history (SFH), the nature of the energy sources that ionizes the gas and search for the existence of inflowing or outflowing gas associated with the AGN and/or other mechanism, like cooling flows, for the central kpc of NGC 5044.

Table 1. Basic parameters of NGC 5044.

Parameter	NGC 5044
RA (2000)	$13^h15^m24^s.0$
Dec.	$-16°23'09''$
Morphology	E0
B (mag)	11.83
M_B (mag)	−22,39
A_v (mag)	0.192
Radial velocity[a] (km s^{-1})	2782
Distance (Mpc)	37
Redshift (z)	0.009 280
L_x [b] (erg s^{-1})	6.8e+39

Data available in NED.[1]
[a]Radial velocity measured by Ogando et al. (2008).
[b]X-ray luminosity in 0.38 keV (Liu 2011).

This paper is structured as follows: in Section 2, we describe the observations and data reduction procedures. Details of the spectral synthesis method and its results are presented in Section 3. In Section 4, we analyse the gas kinematics. The emission gas and its ionization mechanism are studied in Section 5. We show the velocity field model and estimate the black hole mass in Section 6. The geometry and the origin of the observed gas are discussed in Section 7. Lastly, we present our conclusions in Section 8.

2 OBSERVATIONS AND DATA REDUCTIONS

NGC 5044 was observed on 2013 May 04 with the Gemini South Telescope using the GMOS in the IFU mode (Allington-Smith et al. 2002; Hook 2004) using the one slit set-up. In this configuration, the spectrograph uses 500 hexagonal microlenses centred on the object, and other 250 microlenses, separated by 1 arcmin from the object, to simultaneously measure the sky emission. These microlenses, located at the focal plane of the telescope, divide the image in slices with a diameter of 0.2 arcsec and are connected to a set of fibres. This set-up produces a data cube with one spectral dimension and two spatial dimensions with a field of view of 3.5 × 5 arcsec^2. We used the B600-G5323 grating, with a central wavelength of 5620 Å. The spectra covered a range from 4260 to 6795 Å with a 1.7 Å resolution, obtained from the full width at half-maximum (FWHM) of CuAr arc lamp lines. In Table 1, we list some of the general parameters of NGC 5044. Flat-field exposures, bias and CuAr lamp spectra were obtained for calibration and correction of the data cubes. The DA white dwarf EG 274 (Hamuy et al. 1992) was used to perform the spectrophotometric calibration. The seeing value of the observation was measured in the acquisition r image obtained with the GMOS imager (SDSS system). This value and other observation parameters are shown in Table 2.

We followed standard procedures to reduce the data, using IRAF (Tody 1986, 1993) and the tasks contained in the GEMINI IRAF package, as described in detail in Ricci, Steiner & Menezes (2014). The data cube was built with a spatial sampling of 0.05 arcsec, resulting in an FoV with 66 × 98 spaxels. The high spatial frequency noise was removed with a BUTTERWORTH FILTER (Gonzalez & Woods

[1] The NASA/IPAC Extragalactic Database (NED) is operated by the Jet Propulsion Laboratory, California Institute of Technology, under contract with the National Aeronautics and Space Administration.

Table 2. Observation log.

Parameter	NGC 5044
Observation date	2013 May 04
Gemini Programme	GS-2013A-Q-52
Seeing (arcsec)	∼0.7
Airmass	1.14
T_{exp} (s)	1800

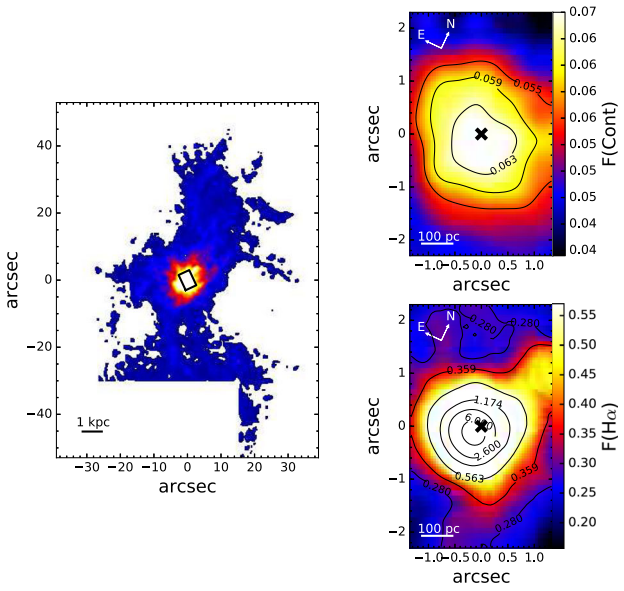

Figure 1. Flux maps for NGC 5044. Left: H α+[N II] emission obtained with NTT+EFOSC2 (Macchetto et al. 1996). The black rectangle represents the GMOS-IFU FoV (5 × 3.5 arcsec^2). Upper right: GMOS-IFU mean continuum image obtained in the spectral range: 4730–4780 Å. Lower right: GMOS-IFU H α map. GMOS maps are in units of 10^{-15} erg cm^{-2} s^{-1} Å^{-1}.

2002; Ricci et al. 2014) using order $n = 6$ and a cut-off frequency Fc= 0.13 FNy, where FNy = 0.5 spaxel^{-1} is the Nyquist frequency. This cut-off frequency was chosen to remove only spatial frequencies higher than the seeing. In addition, the principal component analysis tomography (Heyer & Schloerb 1997; Steiner et al. 2009) was applied in order to remove signatures of low spatial and spectral frequency (Ricci et al. 2014). To correct the atmospheric refraction effects, we applied the equations proposed by Bönsch & Potulski (1990) and Filippenko (1982).

The data cube spectra were corrected for Galactic extinction using the Cardelli, Clayton & Mathis (1989) extinction curve (CCM) for an $A_v = 0.192$ (Schlafly & Finkbeiner 2011) and by Doppler effect using the radial velocity of 2782 km s^{-1} given by Ogando et al. (2008). These authors derived the radial velocity through the cross-correlating technique by using the RVSAO package (Kurtz & MinK 1998) with stellar spectra of G and K giant stars.

We show in the left-hand panel of the Fig. 1 an H α+[N II] emission image of NGC 5044 obtained with NTT+EFOSC2 (Macchetto et al. 1996), where the black rectangle in the middle represents the GMOS FoV. In the right-hand panel, we presented two images extracted from our data cube. The continuum image was obtained by estimating the mean value over the wavelength range between 4730 and 4780 Å, with the continuum peak defined as the photometric centre of the galaxy. We also show the H α image with contours drawn to highlight the extended ionized gas filaments. It is clear from these maps that the morphology of the continuum and H α are distinct and suggests that the ionized gas follows the larger kpc scale filamentary structure, while the continuum follows the stellar distribution.

The wavelength calibration uncertainty was estimated from the arc lamp lines (see Section 4). The spectroscopic standard star was not observed at the same night as the galaxy and this might have affected the accuracy on the absolute flux determination, given 30 per cent of uncertainty in their values. It is worth mentioning that the emission-line flux ratios, used to build the diagnostic diagrams, were not affected by the systematic flux uncertainty, since each used ratio were measured over nearby emission lines. Nevertheless, we check uncertainties for [N II] λ6584/H αλ6563 and [O III] λ5007/H βλ4861 ratios in several spaxels and found a deviation of 3 per cent. The instrumental dispersion was obtained from the FWHM of the CuAr arc lamp, and we used it to correct the velocity dispersion. We noted that the deviation are larger in blueward than in redward, given uncertainties of ∼8 per cent and ∼4 per cent, respectively.

3 STELLAR POPULATION DISTRIBUTION

In order to obtain the SFH and to analyse the gas emission free from the stellar population contamination, we performed stellar population synthesis spaxel by spaxel. Therefore, we use the STARLIGHT code (Cid Fernandes et al. 2004, 2005; Mateus et al. 2006; Asari et al. 2007; Cid Fernandes et al. 2009), which essentially fits the whole underlying observed spectrum, O_λ, with a model spectrum, M_λ. To create a model spectrum, M_λ, the code finds a combination of $N_\star$ simple stellar populations (SSPs) resulting in a final population vector $\boldsymbol{x}$, whose components represent the fractional contribution of each SSP to the total synthetic flux at wavelength λ_0 (Cid Fernandes et al. 2004, 2005). Extinction is parametrized by the V-band extinction A_V and modelled by STARLIGHT as due to foreground dust. In summary, the code solves the following equation:

$$M_\lambda = M_{\lambda 0}\left[\sum_{j=1}^{N_\star} x_j b_{j,\lambda} r_\lambda\right] \otimes G(v_\star, \sigma_\star), \quad (1)$$

where $M_{\lambda 0}$ is the synthetic flux at the normalization wavelength, $G(v_\star, \sigma_\star)$ is a Gaussian function used to model the line-of-sight stellar velocity distribution, which is centred at velocity $v_\star$ with dispersion $\sigma_\star$. The term x_j is the jth population vector component of the base set, $b_{j,\lambda}$. The spectra of the SSP of the base of elements are normalized at λ_0, the reddening term is represented by $r_\lambda = 10^{-0.4(A_\lambda - A_{\lambda 0})}$. The final fit is carried out by minimizing a χ^2 equation. The robustness of the fits can be measured by the STARLIGHT output parameter ADEV, which is the average deviation over the fit of pixels $|O_\lambda - M_\lambda|/O_\lambda$.

It is clear from the above discussion that the most important ingredient in stellar population synthesis is the SSPs used in the fit (what we call base set). We used SSPs taken from Bruzual & Charlot (2003) models. These models were chosen because they are the most adequate to fit our data, since they have a spectral resolution of 3.0 Å, that is close to our data spectral resolution (see Section 4) and do offer enough spectral coverage (3200–9500 Å) to fit our data. Besides they do provide an adequate number of SSP in order to have all the possibilities of ages and metallicities found in galaxies. In addition, we decided to use the BC03 models because they are widely used, thus allowing for comparison with published results. These models are computed using the isochrone synthesis code developed by BC03 and are divided in 221 spectra with ages between 0.1 Myr and 20 Gyr for a wide range of metallicities. These

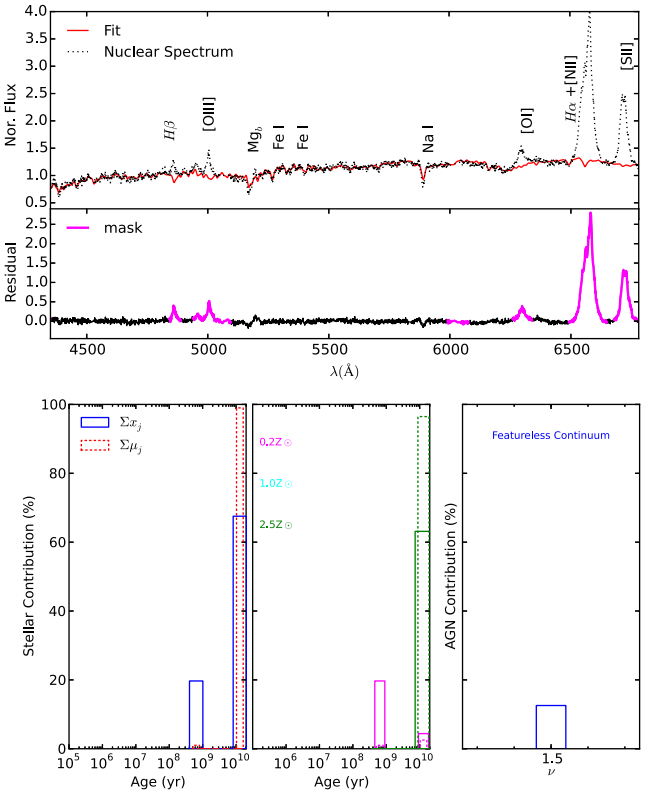

Figure 2. Example of fits. Top panel: the observed and modelled spectra normalized to unity at 4755 Å, central panel: residual spectrum. The masked regions are in magenta and the residual spectrum in black lines. At the bottom, we show the contribution of the stellar population vectors in light fractions (x_j, full line) and mass fractions (μ_j, dashed line). Left: metallicities summed contributions, centre: contributions separated by each metallicity, right: FC contribution.

models mainly use the BaSeL 3.1/STELIB libraries, with a spectral resolution of 3 Å (STELIB) in the optical region. Following Dametto et al. (2014), our final base set was selected in order to have enough, representative and not degenerated elements, covering seven ages ($t = 0.6, 0.9, 1.4, 2.5, 5, 11$ and 13 Gyr) and three metallicities (0.2, 1 and 2.5 $Z_\odot$). In the fits, the spectral resolution of the data was resampled to match the models. The Cardelli et al. (1989) extinction law is typically used to fit the extinction data both for diffuse and dense interstellar media. Since we are fitting a LINER-like spectrum galaxy, we additionally included a featureless continuum (FC) in the form of a power law ($F_\nu \propto \nu^{-1.5}$) in order to account for a possible non-thermal contribution (e.g. Cid Fernandes et al. 2005; Riffel et al. 2009, and references therein).

To map the whole FoV, the stellar population fits were performed for each one of the spaxels. The nuclear region (∼200 pc) was defined as the one where a broad component was detected on H α emission. Fig. 2 shows the fit of the spectrum at the nuclear spaxel, defined as the location of the continuum peak. The emission lines and the final continuum fit are also shown. The percentage contribution of each age (in mass[2] and light fractions) and FC to the final fit are presented in the bottom panels. Here, we discuss only the light fractions, since it is the parameter we derive directly and where larger differences are observed (in terms of mass, the emission is completely dominated by the old stellar population that has a high M/L).

[2] The mass fractions are obtained using the M/L ratios for each SSP, see STARLIGHT manual for details.

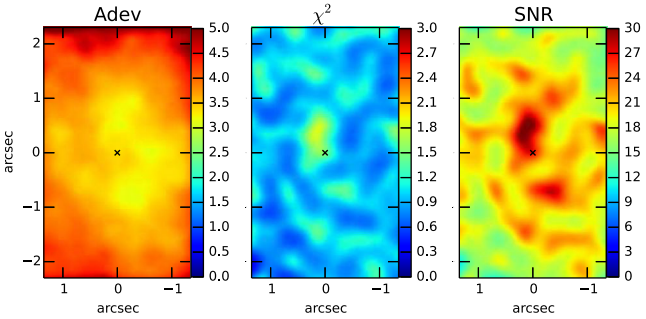

Figure 3. Quality of the fit maps. Left: percent mean deviation, centre: χ^2 and right: SNR. For details, see the text.

The quality of the fit over the whole FoV can be seen in Fig. 3 where the parameters ADEV and χ^2 are shown. In this figure, we do also show a signal-to-noise ratio (SNR) map. It is clear from this map that even for the borders of the FoV an SNR >15 is found. It is worth mentioning that according to tests presented by Cid Fernandes et al. (2004), for spectra with values of SNR > 10 STARLIGHT does properly reproduce the input parameters, thus producing reliable results for the stellar populations fits. However, the strengths of the Mgλ5143 and Naλ5894 lines are not well reproduced by our fitting, possible due to the fact that the BC03 models do not consider α enhancement processes. In addition, the NaD doublet has contribution of the ISM. Due to this fact we have tested the stellar population fits in three cases, with and without removing both the NaD and Mgλ5143 lines form the fit and only removing the NaD doublet. We have not found any significant difference between both fits. In both cases, less than ∼10 per cent of these lines strength was not reproduced by the fitted model. Likely the NaD residual seen in Fig. 2, is due to ISM contribution present in the nucleus of NGC 5044 (see e.g. Ferrari et al. 1999). As discussed in Davis et al. (2012), the blueshifted NaD doublet provides a good probe of the cold interstellar medium outflow. In the case of NGC 5044, we have not found any blueshifted component for NaD doubled in all our FoV, indicating that in this galaxy, the cold material is probably not outflowing.

Interestingly, our fitting resulted only in contributions of four of the base components: three SSPs with ages 900 Myr (0.2 $Z_\odot$) and 13 Gyr (0.2 and 2.5 $Z_\odot$), plus an FC component. The 2D maps for these components (in light fractions), together with mean age, A_v, FC and mean metallicity are shown in Fig. 4. It is clear from this figure that the light in the central region of NGC 5044 is dominated by an old stellar population. Besides it is also clear that an intermediate age (900 Myr) stellar population is present, surrounding the galaxy nucleus. As far as we know, the presence of stellar populations with these ages (900 Myr) in the nuclear region of elliptical galaxies is not a common trend. For example, from an extensive stellar population study performed with large field data of the CALIFA survey, González-Delgado et al. (2015) found that in average the S0 and E galaxies have a dominant stellar population with almost the same age and they are older than those found in spirals. In addition, they reported for elliptical galaxies a small variation on the stellar ages along the galaxy radii (from 10^{10} to $10^{9.7}$ yr from the centre to 3 half-light radius (see fig. 17 of González-Delgado et al. 2015). The differences in the results found by González-Delgado et al. (2015) and ours may be due to the spatial and spectral resolution probed by GEMINI GMOS. For instance, the presence of spatially resolved circumnuclear intermediate age stellar populations, like we found in NGC5044, was reported for the bulges of spiral Seyfert galaxies (Riffel, Storchi-Bergmann &

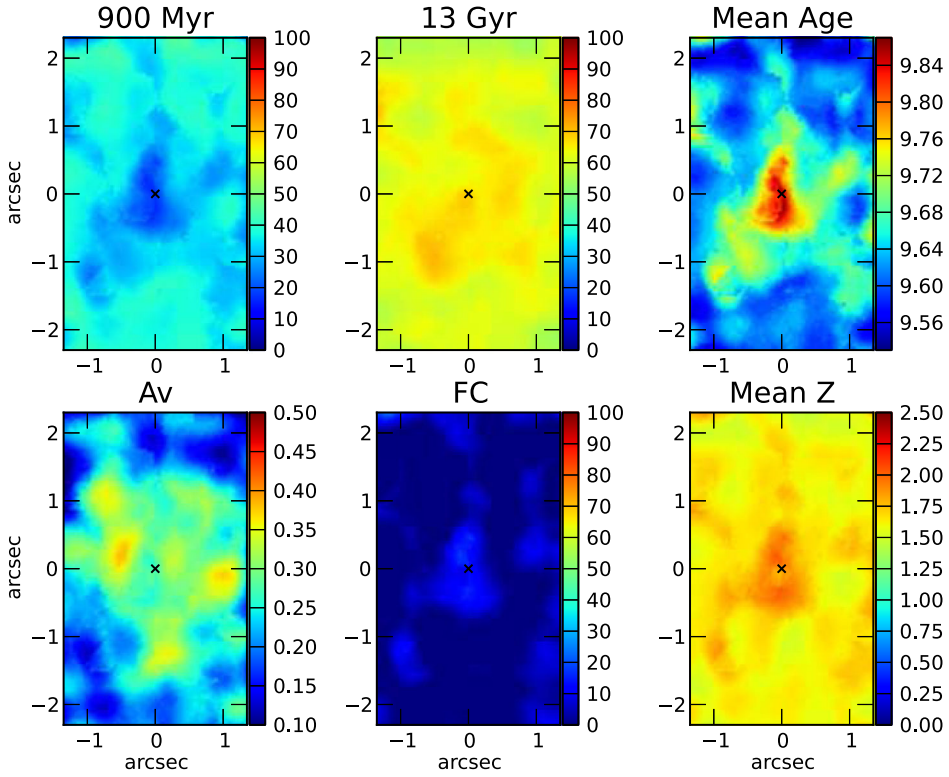

Figure 4. Top panel shows the population maps of NGC 5044 at age, whereas in the left we can see the population contribution of 900 Myr, in the centre is the population contribution of 13 Gyr and at right is the mean age. The bottom panel shows A_v map at left, the FC contribution in the centre and the mean metallicity (Z) at right

Nagar 2010; Riffel et al. 2011; Storchi-Bergmann et al. 2012). The maps of mean age and mean metallicities show a trend consistent with the stellar population becoming more metal rich and older with decreasing distance with respect to the galaxy centre. Some studies have shown that the stellar population in early-type galaxies also become progressively more metal rich and older with increasing velocity dispersion (Thomas et al. 2005; Clemens et al. 2006, 2009). Indeed, we found higher σ values in the central region of the NGC 5044 (see Section 4), thus our result does further support the findings by these authors.

In addition, our stellar population results are in agreement with the results found by Rickes et al. (2004), who performed stellar population synthesis using optical long slit data in a much larger spatial scale than ours. These authors used two different bases of elements, one with three components with metallicities $[Z/Z_{\odot}] = 0$, -0.4 and -1.1 and age $= 10^{10}$ yr, and another with solar metallicity and ages with 10^{10}, 10^{8} and 10^{6} yr. They noted that there was an improvement on the fit when considering different metallicities over the different ages, with the more metallic component dominating in the central region, while the lower metallicities were enhanced in the outer regions.

Literature results on the stellar content of NGC 5044, as those presented by Werner et al. (2014) based on the *GALEX* and *WISE* data report an unusual star formation rate in NGC 5044 (SFR $=$ 0.073 $M_{\odot}$ yr^{-1}, using a region of 10 kpc, over the last 1 Gyr). Besides David et al. (2014) suggested that the unusual lines of PAHs found in NGC 5044 and the uncertainty in the stellar age are consequences of episodes of star formation that occurred in the last 1 Gyr (Marino et al. 2011). These results are further supported by our finding, that there is a significant contribution of the 900 Myr stellar population, distributed along the centre of the galaxy (reaching values of ∼50 per cent at some locations).

We also found an FC contribution of about 20 per cent in the nuclear region. This component is consistent with a scenario where the gas in the nuclear region is ionized by a weak AGN. However, we find some significant contribution of the FC in the external regions. Since this component is degenerated with a young reddened stellar population we interpret this contribution as being related with the fact that BC03 models do not include blue horizontal branch stars, and STARLIGHT fits tend to choose a young population to account for this blue population (see Cid Fernandes & Gonzalez-Delgado 2010, for details).

The visual extinction map (A_v) shows a clear enhancement at the galactic centre, reaching ∼0.35 mag and decreasing to 0.1 mag at the external region. Ferrari et al. (1999) found a mean extinction $A_v = 0.01$ (mag) within a region of 10arcsec, which is about twice of the size of our region. From this A_v, they estimated a dust mass of about 10^4 $M_{\odot}$ distributed irregularly along the galaxy. In addition, a hot dust mass of 67 $M_{\odot}$ was determined by Ferrari et al. (2002) from Mid-IR data.

4 KINEMATICS OF IONIZED GAS

In order to map the gas kinematics, we measured the centroid velocity (hereafter velocity field, v_r) and velocity dispersion (σ_{v_r}) from the data cube without the subtraction of the stellar populations contribution (see Section 3), because the stellar population templates have slightly lower resolution than the data cube, this difference would affect the accuracy on velocities determination. We have used an in-house fitting code (Hernandez-Jimenez et al. in preparation) to fit Gaussian functions to the emission-line profiles. We fitted single- or multi-Gaussian components to the spectra in order to obtain the flux of each emission line. The line pseudo-continuum is linearly fitted using side-bands regions, free from emission or

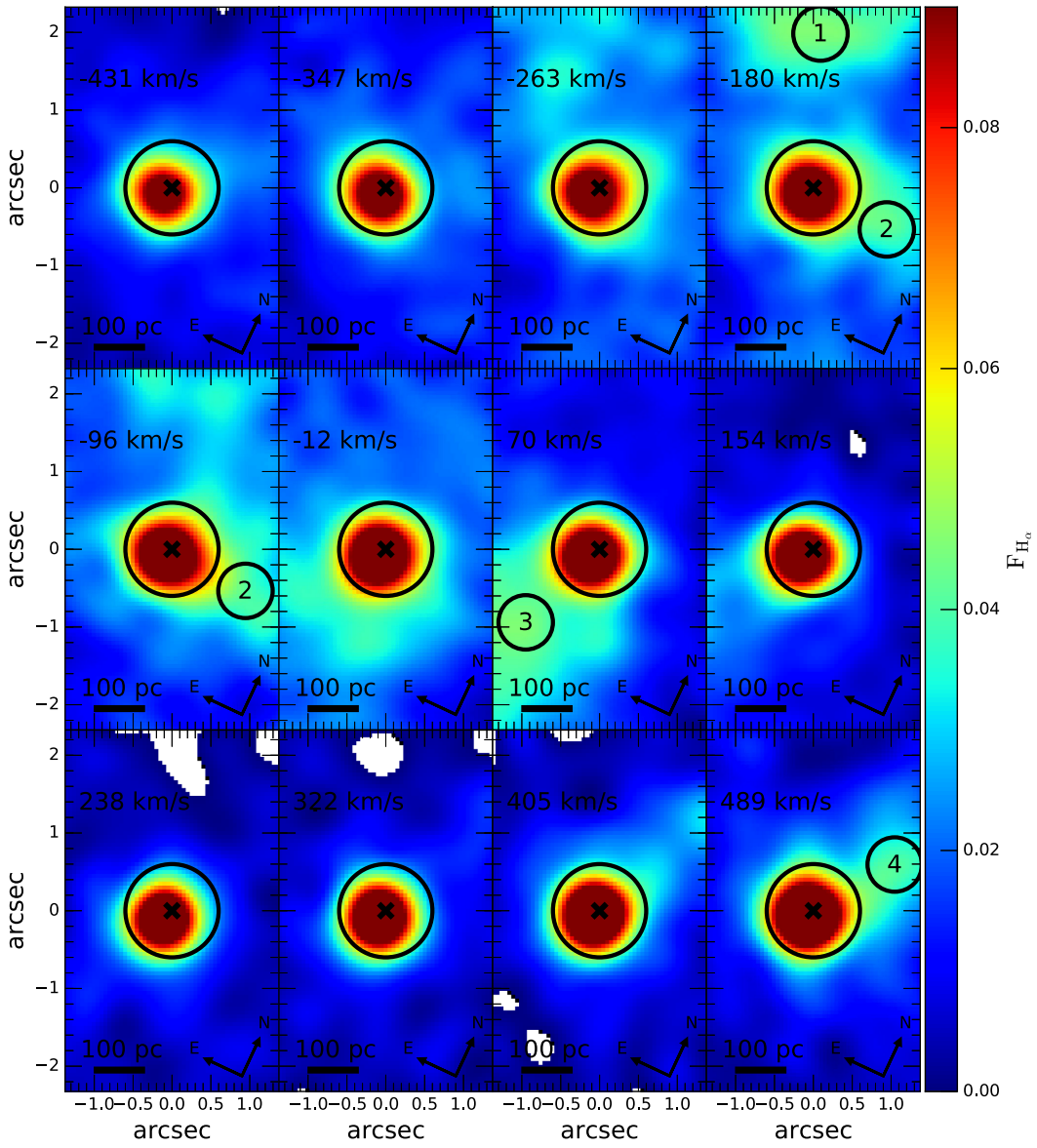

Figure 5. Velocity channels along the Hα emission line in $\sim$80 km s^{-1} bins centred on the velocities indicated in each panel. The intensities are represented in the colour scale to the right in flux units of 10^{-15} erg cm^{-2} s^{-1}. The central circle in all channels represents the nuclear region. The photometric centre of the galaxy is marked with a symbol 'x' in all channels.

absorption features, as close as possible to the emission line. The uncertainty associated with the measurements of the velocity field (δ_{v_r}), in a given line at λ_0, depends implicitly on the error of the Gaussian peak centroid, (δ_{λ_0}). Then, we do a straightforward error propagation of the basic expression for the Gaussian peak centroid (λ_0) to calculate δ_{v_r}. We derived the following expression:

$$\delta_{v_r} = \frac{c}{\lambda_0}\delta_{\lambda_0};\ \delta_{\lambda_0} = \frac{I_0\sqrt{N}}{F_\lambda}\delta_\lambda, \tag{2}$$

where I_0 is the intensity at maximum of the fitted Gaussian, N is the number of pixels, F_λ is the line flux and δ_λ is the error of the spectral dispersion taken from the FWHM (1.7 Å) of the CuAr arc lamp. The error map δ_{v_r} of Hα line is shown in panel (d) of Fig. 10, where we can see that the uncertainties in velocity field in the nuclear region is lower than 10 km s^{-1}, while at the data cube border (where the SNR is lower), the error is $\sim$20 km s^{-1}.

In order to study the kinematic components of the ionized gas in the circumnuclear region of NGC 5044, we obtained channel maps between -431 km s^{-1} and $+489$ km s^{-1} relative to the systemic velocity of the galaxy derived by modelling the gas velocity field (see Section 5 and Table 4), in velocity bins of 80 km s^{-1} (see Fig. 5). We identified, in the negative channel map -180 km s^{-1}, a bright structure at NE, named as region 1, and a weak structure (region 2) at west, which is also observed at the channel -96 km s^{-1}. In the positive channel maps, the most conspicuous structure was named as region 3 and is located at south, at the channel 70 km s^{-1}. There is also a filamentary structure, region 4, located at north between 405 and 489 km s^{-1}. Comparing these ionized gas structures with the ones of molecular gas identified by David et al. (2014), using ALMA observations, we found that the brighter peak located at NE of the channel map -180 km s^{-1} matches with the approaching cloud 13 (see fig. 6 in David et al. 2014), whereas the south filament in channel map 70 km s^{-1} coincides with the receding molecular

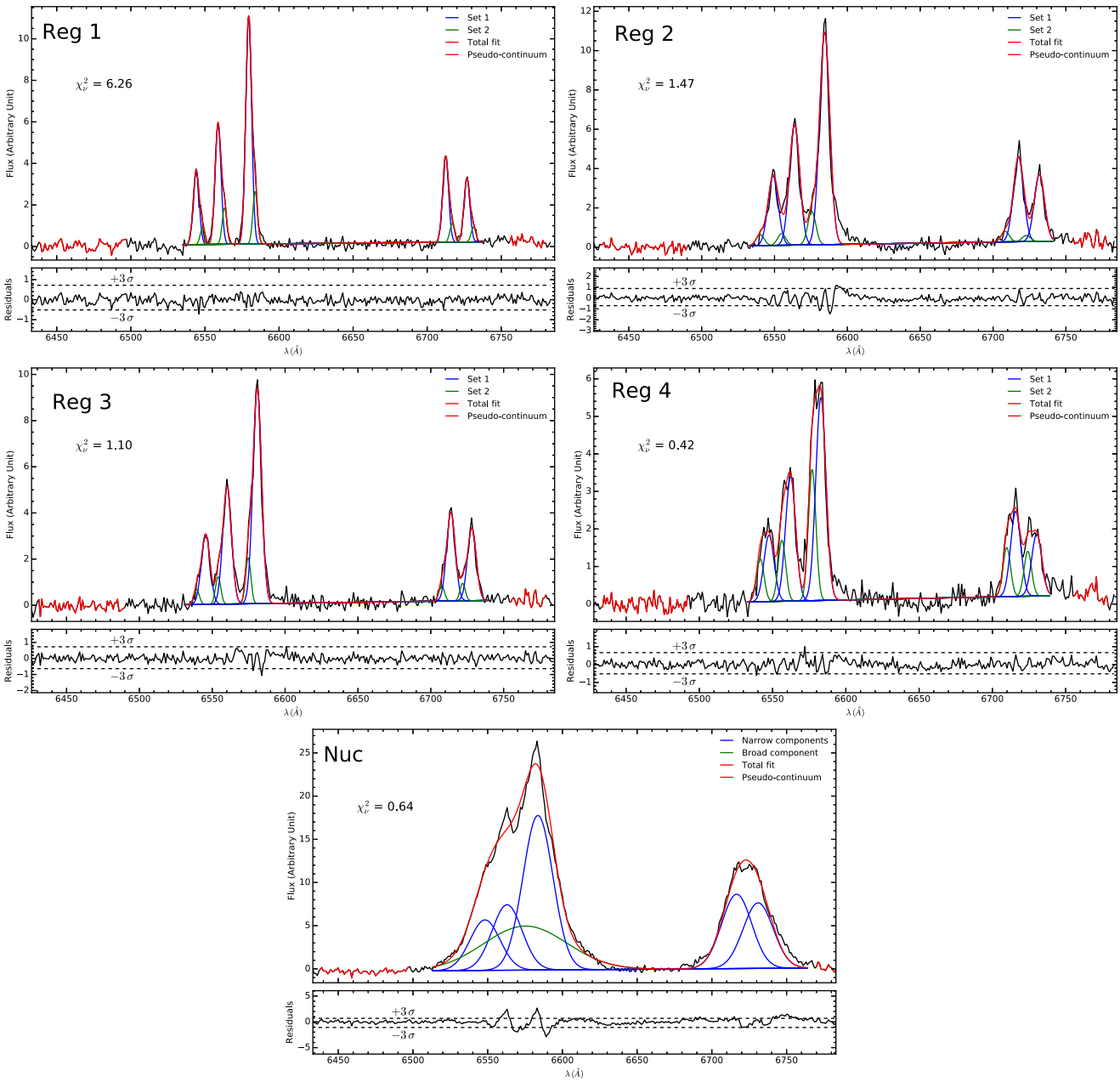

Figure 6. Line profiles of [N II] λ6548, H α, [N II] λ6583, [S II] λλ6717,31 obtained in the apertures of ∼0.7 arcsec. The profile of the nuclear aperture shows components with FWHM ∼1080 km s^{-1} and an H α broad component (FWHM ∼ 3000 km s^{-1}). The emission-line profiles obtained in the other regions are composed by two set of narrow lines (FWHM < 400 km s^{-1}).

gas cloud 18. In both regions, David et al. (2014) found evidence that the molecular gas is falling into the centre of the galaxy. On the other hand, we point out that the central region appears in all channel maps, indicating the presence of a nuclear broad component with an FWHM ∼ 3000 km s^{-1}, typical of AGN.

We fitted the [N II]+H α complex at the nuclear region with six Gaussians, five corresponding to the narrow components of the lines [N II] λ6548, H αλ6563, [N II] λ6583, [S II] λλ6717,31 and one to account for the H α broad component. We constrained the narrow components as having the same redshift and FWHM for all lines, and fixed [N II] λ6583/[N II] λ6548 = 3.1 (Osterbrock & de Robertis 1985). The fit for the additional component was done with all parameters free, resulting in a large FWHM value (∼3000 km s^{-1}), thus we associated it with a broad H α emission. To properly reproduce the emission-line profiles of the outer regions (1–4), it was necessary to have two sets of Gaussians, constrained as mentioned above, but each set with their own values for redshift and FWHM. We only considered lines with SNR above than 3σ of the fitted continuum (see Fig. 6). In Table 3, we show the values obtained for each fit, where V_c is the peak velocity of the line, and $|\Delta V|$ is the shift between the line sets. The fitted H α+[N II] and the [S II] line profiles, obtained with the apertures of the 0.7 arcsec, are shown in Fig. 6. The secondary set of lines of regions 2, 3 and 4 are blueshifted with respect to the first one. The difference

Table 3. Results for the Gaussian profile fits measured for Hα emission line in selected regions.

Region	Set	FWHM (km s^{-1})	V_c (km s^{-1})	$\lvert\Delta V\rvert$(km s^{-1})
1	1	215 ± 28	−178 ± 34	196 ± 50
	2	172 ± 25	18 ± 37	
2	1	376 ± 40	46 ± 25	407 ± 37
	2	301 ± 35	−361 ± 28	
3	1	323 ± 36	−119 ± 28	283 ± 44
	2	194 ± 27	−402 ± 35	
4	1	376 ± 40	−23 ± 25	274 ± 39
	2	280 ± 33	−297 ± 30	
Nuc	Narrow	1076 ± 68	5 ± 15	558 ± 17
	Broad	3001 ± 113	562 ± 9	

in velocity between the sets for region 2 is 407 km s^{-1}(the largest one). We point out that this region is the closest from the nucleus. The velocity difference for regions 3 and 4 are ∼300 km s^{-1}. The secondary set of lines for region 1 is redshifted with respect to the primary one in about 200 km s^{-1}. Fig. 6 also shows the line profiles for the nuclear region, where the Hα broad component is blueshifted with respect to the narrow component by 558 km s^{-1}. The FWHM of these components are ∼1080 and ∼3000 km s^{-1}, respectively. It is clear from Fig. 6 that the regions 2 and 4 do present a wider FWHM than regions 1 and 3. Besides they do show a weak red wing in the [N II]+Hα complex (very close to the 3σ detection limit). We do not have a very clear explanation for this component; however, we do speculate that this weak component is most likely originated from material outflowing from the AGN, once these two locations are closer to the galaxy centre. Similar results were found for other early-type galaxies, for example, Ricci et al. (2014) fitted two sets of Gaussians to the emission lines in the inner 100 pc of 10 early-type galaxies and found that for seven galaxies one of these sets has FWHM > 390 km s^{-1}and the other (which corresponds to the Hα broad component) has FWHM > 2000 km s^{-1}. In summary, this exercise indicates that there are three kinematical components that we discuss in the following sections.

Velocity field and dispersion maps measured on Hα are shown in Fig. 10. They were obtained from a fit of a single component for each emission line over the whole FoV, except for the nuclear region where a very broad component was added. Analysing the velocity field map, we found evidence of rotating gas and that the velocity field is asymmetric,[3] with the receding side at the south and approaching side at the north. The maximum approaching value is −120 km s^{-1} at ∼200 pc and the receding one is ∼200 km s^{-1} at ∼100 pc. The line of nodes lies in PA ∼ 152°.

The Hα velocity dispersion map corrected by the instrumental broadening (σ, Fig. 10e), shows a large range of values (with a constant mean uncertainty of 4 km s^{-1}) of through the overall FoV, from 100 up to 600 km s^{-1}, the peak of the distribution has an offset of ∼30 pc to SE with respect to the photometric centre, marked with a symbol 'x' in all maps. Two different regions can be clearly distinguished from the distribution of σ values. The first one is the nuclear region that shows a σ gradient from 300 to 600 km s^{-1}. The second region presents a 'dove-like' distribution of σ values between 150 and 300 km s^{-1}, with 'wings' on the east and north directions and the 'body' in the SW direction. We noted that, in the rest of the FoV, the velocity field and dispersion velocity have similar values (∼100 km s^{-1}).

[3] This asymmetry can be due to the non-rotational motions of the filamentary structure observed in this galaxy, see Section 7.

5 DISTRIBUTION AND IONIZATION MECHANISMS OF THE IONIZED GAS

The results of the individual fits obtained from the stellar synthesis can be subtracted spaxel by spaxel, letting us with a clean residual data cube, free from the stellar population absorption features (see bottom, Fig. 2), thus, allowing us to study the pure emission gas component. To measure the emission-line fluxes we used the same methodology described in Section 4.

Fig. 7 presents the ionized gas flux distribution for following emission lines: Hα total flux, [N II] λ6583, [S II] λ6717+λ6731 and [O III] λ5007. In the inner 1 kpc of the NGC 5044, the gas distribution is irregular. The flux maps for the emission lines [N II] and [S II] show that their emissions are more concentrated at the nucleus and indicate a preference of distribution along south–north direction, while the [O III] map shows emission over the whole FoV, with regions of higher intensity extended along the EW direction. Also, the flux distribution for other emission lines detected in our data (Hβ, [O III] λ4959 and [O I] λ6300), do have a lower SNR and are shown for completeness.

From the flux maps, we derived the following values for the emission-line ratios: $0.1 < \log$ ([N II] λ6583/Hα) < 0.5, $-0.05 < \log$ [S II] λλ/Hα < 0.5 and $-0.4 < \log$ [O III] λ5007/Hβ < 0.5, which are typical of LINER-like emission-line objects (Heckman 1980; Ho 2008).

The dominant ionization/excitation mechanism of the ionized gas in NGC 5044 is still controversial. According to Macchetto et al. (1996) the observed spectra can be explained by post-AGB stars, while Rickes et al. (2004) suggest that the spectra have contributions of an LLAGN in the nuclear region plus post-AGB stars in the outer parts.

In order to study the dominant ionization mechanism of the emission-line gas in NGC 5044, we constructed diagnostic diagrams using the emission-line ratios mentioned above. The diagnostic diagrams for the nuclear region and for the regions 1–4 are shown in Figs 8 and 9, respectively.

In the diagnostic diagrams, in order to discriminate among the different excitation mechanisms, we added the theoretical maximum starburst line of Kewley, Heisler & Dopita (2001, hereafter KW01) and the theoretical line separating purely star formation galaxies, Seyferts, LINERs and composite galaxies of Kewley et al. (2006, hereafter KW06 line). The empirical line dividing star-forming galaxies and composite objects of Kauffmann et al. (2003, hereafter KF03) was also included.

Since shocks could explain the LINER-like spectra (Heckman 1980; Dopita & Sutherland 1995; Dopita et al. 2015), we also added to the diagnostic diagrams shock models calculated with the MAPPINGS III shock and photoionization code from Allen et al. (2008). These shock models include a range of chemical abundance sets, pre-shock densities from 0.01 to 1000 cm^{-3}, velocities up to 1000 km s^{-1}, magnetic fields from 10^{-10} to 10 $^{-4}$ G, and magnetic parameters (B/$n^{1/2}$) from 10^{-4} to 10 μG cm$^{3/2}$. Since, the electron density (n_e) of the pre-shock material is an important physical quantity that affects the emission spectrum in radiative shocks, we estimated n_e using [S II]λλ 6717, 6731 emission-line ratios (Osterbrock & Ferland 2006; Panuzzo et al. 2011) measured in the regions 1–4. We found $35 < n_e < 200$, the lower value corresponds to the region 4, while the higher value was found in the region 3, thus we adopted a mean value of $n_e = 100$ cm^{-3}. The models consistent

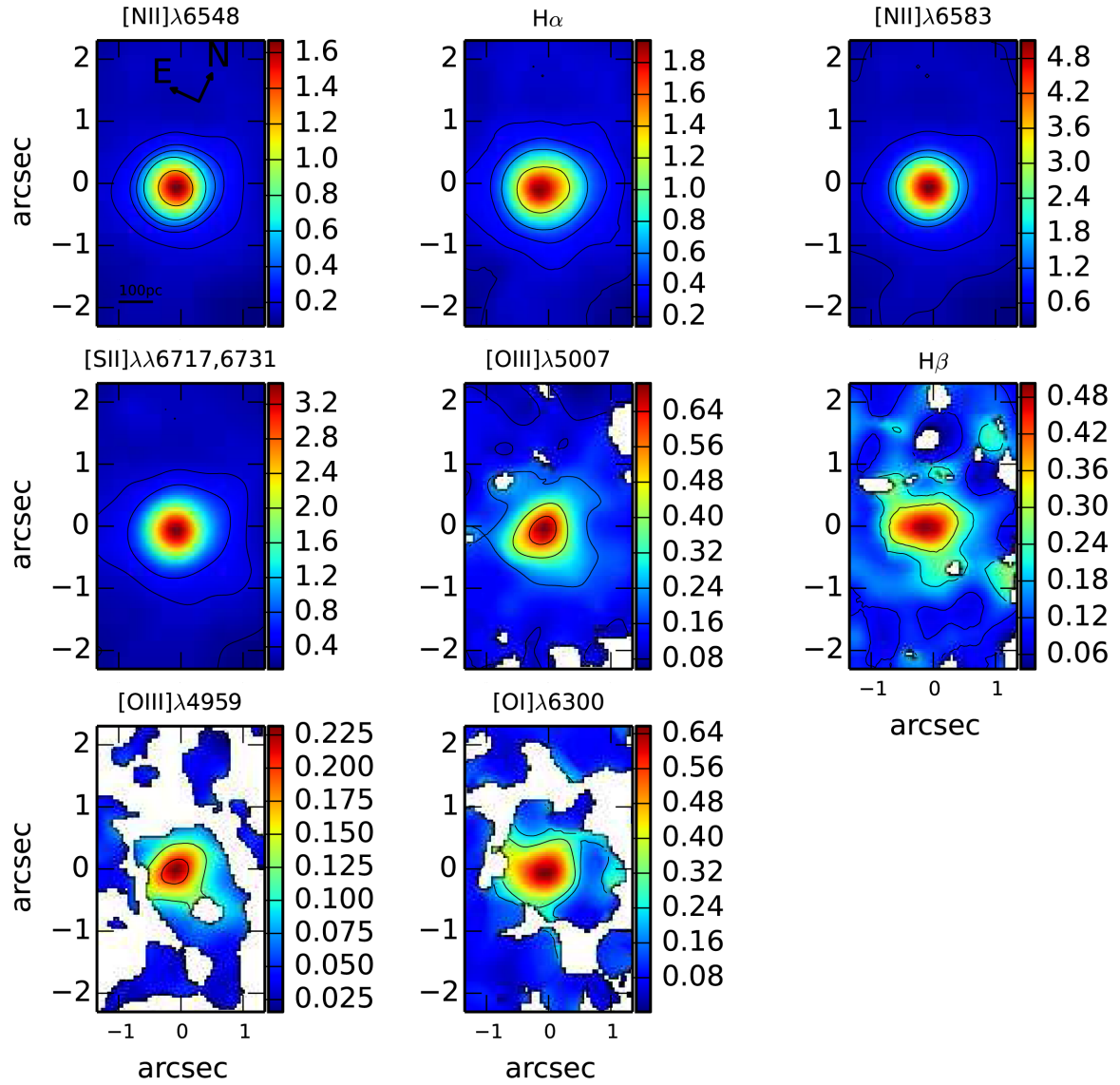

Figure 7. Flux distribution of the emission lines measured from the spectra free from the stellar contribution. The colour bar shows the range of flux values expressed in units of 10^{-15} erg cm^{-2} s^{-1}.

with our observational data are those of shock without precursor, with solar metallicity and with pre-shock density of $n = 100$ cm^{-3}.

In Fig. 8, we show the ratios obtained for all the spaxels along the FoV (yellow) and highlight those of the nuclear region (black). It is clear that the nuclear region presents some discrepancy with respect to the circumnuclear one, suggesting a mixing of ionization mechanisms, since the black circles are in the LINER region, while the circumnuclear (yellow) lies in the shock zone.

In addition, we investigate in detail the excitation mechanism of the selected regions 1–4 identified in the Hα channel maps (Fig. 5). For each one of these regions, we constructed diagnostic diagrams involving the line ratios [O III]/Hβ × [S II]/Hα and [O III]/Hβ × [N II]/Hα (Fig. 9). For the diagnostic diagrams using the [S II]/Hα ratio (which is more sensitive to shocks), we found shock velocities >550 km s^{-1}, while the shock models for [N II]/Hα are not able to predict the observed values for regions 1, 3 and 4. However, region 2 can be explained by models with velocities of ∼400 km s^{-1}, for the [N II]/Hα ratio. The above results suggest that the dominant excitation mechanism in the identified regions is compatible with shock waves with velocity >550 km s^{-1} (for the [S II]/Hα ratio) moving in an environment with density of $n_e = 100$ cm^{-3}. Therefore, in the inner kpc of this galaxy there are two ionization mechanisms taking place: in the centre (∼200 pc) the emission lines are dominated by photoionization due to an LLAGN, while in the circumnuclear region the gas emission can be shock dominated. In addition, this result is in agreement with the fact that we are finding a significant fraction of the FC in the central region (see Fig. 2) and with the broad component that we found for Hα (see Fig. 6 Nuc), which indicates the presence of an AGN.

6 THE GAS VELOCITY FIELD OF NGC 5044: DETERMINATION OF THE SUPERMASSIVE BLACK HOLE MASS

In order to understand the gas kinematics, we have modelled the observed velocity field, assuming that the ionized gas follows circular orbits in a plane as proposed by Bertola et al. (1991), summarized

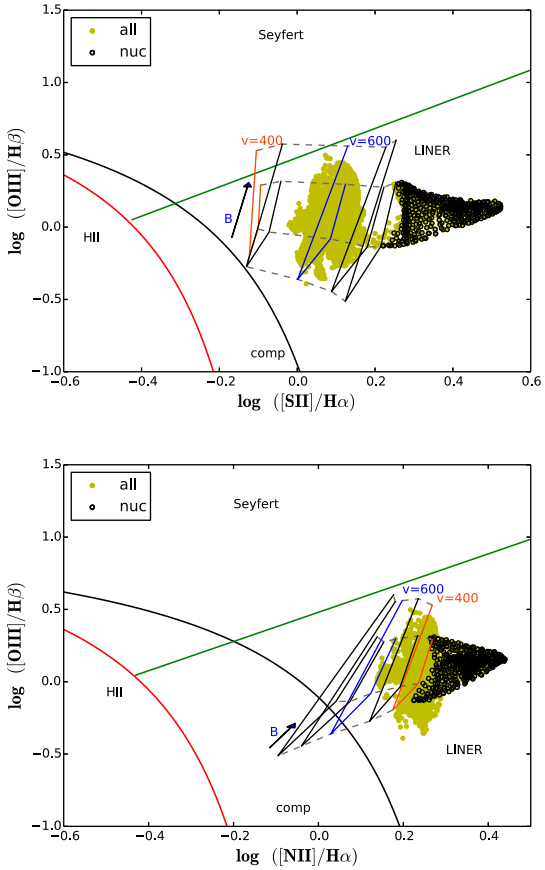

Figure 8. Diagnostic diagrams. Line ratios of all the spaxels are shown by yellow dots. The nuclear regions (∼200 pc) are in black dots. Black (KW01), red (KF03) and green (KW06) lines are the empirically and theoretically derived nuclear activity separations between LINERs, Seyfert and Starbursts. Solid and dashed lines are the grid of the shock models by Allen et al. (2008). The grid has a range in shock velocity (solid line) plotted in steps of 100 km s^{-1}, from 400 up to 800 km s^{-1}, we highlighted $v = 400$ km s^{-1} (red) and $v = 600$ km s^{-1} (blue). The magnetic parameters are plotted as the dashed lines with the values 3.23, 0.5, 1 and 2 μG cm$^{3/2}$.

by the following equation:

$$V(R,\psi) = V_s + \frac{AR\cos(\psi-\psi_0)\sin\theta\cos^p\theta}{R^2[\sin^2(\psi-\psi_0)+\cos^2\theta\cos^2(\psi-\psi_0)]+c_0^2\cos^2\theta^{p/2}}. \quad (3)$$

This results in a velocity curve that increases linearly at small radii and becomes proportional to r^{1-p} for the external regions. R and ψ are the radial and angular coordinates of a given pixel in the plane of the sky; A is related to the amplitude of the rotation curve; c_0 is a concentration parameter. The parameter p defines the form of the rotation curve, varying in the range between 1 (logarithm potential) and 1.5 (Keplerian potential), which is the range of values expected for galaxies (Bertola et al. 1991); the parameter V_s is the systemic velocity; ψ_0 is the position angle of the line of nodes; θ is the disc inclination ($\theta = 0$ for face-on discs); finally, there are two implicit parameters: the coordinates of the kinematic centre, R_{cx} and R_{cy}. Equation 3 has a degeneration between A and θ parameters, which makes not reliable the θ value derived to the fit. Then, we estimated θ of 42° ± 2° from the outer isophotes of the H α flux image. Thus, this parameter was fixed for the fit.

We used a Levenberg–Marquardt method to fit the observed velocity field. The weighted fit was done considering the error map of δ_{v_r} (Fig. 10d). The fitted parameters and their respective errors are given in Table 4. The R_{cx} and R_{cy} are not listed in this table, instead of them, we give the difference between kinematic and photometric centres, in the sky plane, Δx and Δy. The reduced χ^2 of the fit is 10.8, this high value is due to the perturbations of the observed velocity field, and is reflected in the residual map (Fig. 10c), which presents non-rotational strong kinematic components, they are discussed and analysed in detail in Section 7.

The galaxy kinematic centre has a small offset, of 18 pc to NE direction, with respect to its photometric centre. Considering that our angular resolution is ∼125 pc, this offset is negligible and we conclude that the kinematic centre coincides (within the uncertainties) with the photometric nucleus.

The rotating disc model that provided the best fit of the observed velocities is shown in Fig. 10(b). The rotation curve derived from this model is presented in Fig. 11. It is clear that the gas reaches its maximum rotational velocity (240 km s^{-1}) at a distance of 136 pc. In addition, the derived value for the p parameter (p ∼1.5) indicates that the gas distribution has a Keplerian behaviour and thus the dynamic in this region must be dominated by a high-mass concentration. Assuming the Keplerian approximation for the gas motion ($M = r \times V_{\rm rot}^2/G$), we estimate a mass of 1.9 ± 0.9 × 10^9 M$_\odot$ within the inner 136 pc.

The value of this mass concentration can be verified using the M–σ relation (Kormendy & Ho 2013) as follows:

$$M_{\rm bh} = 0.309^{+0.037}_{-0.033} \times 10^9\,{\rm M}_\odot \left(\frac{\sigma_\star}{200\,{\rm km s^{-1}}}\right)^{4.38\pm0.29}, \quad (4)$$

where $\sigma_\star$ is the stellar velocity dispersion measured in an aperture with radius of R_e/8, with R_e being the half-light radius. We derived this radius for NGC 5044 from its brightness surface profile, using a K_s-band image taken from 2MASS Extended Source Image Catalogue (Skrutskie 2006). The obtained value is R_e = 29 arcsec, which corresponds to 5.1 kpc, the required value of R_e/8 is ∼600 pc, which is close to the data cube FoV. The $\sigma_\star$ was determined from the absorption lines Mgbλ5167, FeIλ5270 and FeIλ5335 measured in a single integrated spectrum obtained collapsing all the non-stellar subtracted cube spectra, since we are only interested to measure the FWHM of these stellar lines. The FWHM of the lines was corrected for instrumental broadening. The resulting $\sigma_\star$ is the mean weighted by the flux of each absorption line, and the uncertainties were estimated from the standard deviation of these measurements. Then, the found value of $\sigma_\star$ for NGC 5044 is 300 ± 57 km s^{-1}. This value is in agreement with the 250 km s^{-1} found for the galaxy centre in Caon et al. (2000). The $M_{\rm bh}$ derived using this $\sigma_\star$ is 1.8 ± 1.6 × 10^9 M$_\odot$, which is in full agreement with the value obtained with the Keplerian approximation.

With the purpose of testing the possibility that the peculiarities in the velocity field obtained in Section 4 [e.g. a steep rise towards the centre (300–600 km s^{-1}), and the rotation curve reaching its maximum value at a small radius (136 pc)] are associated with the presence of a black hole, we plotted in Fig. 11 the Keplerian rotation curve expected for an Supermassive Black Hole (SMBH) with M = 1.8±1.6 × 10^9 M$_\odot$ (dash–dotted line), the observed (red line) and modelled (black line) rotation curves for the central region of the galaxy. We also include the rotation curve derived from the Sérsic profile (dashed line) using the K-band brightness surface profile (see Hernandez et al. 2013, 2015, for details on methodology). From Fig. 11, it is clear that for the inner 136 pc (dashed vertical line), the central kinematics is dominated by the SMBH potential. This would explain why the maximum rotation curve of the gas and the steep rise in the dispersion velocity profile is

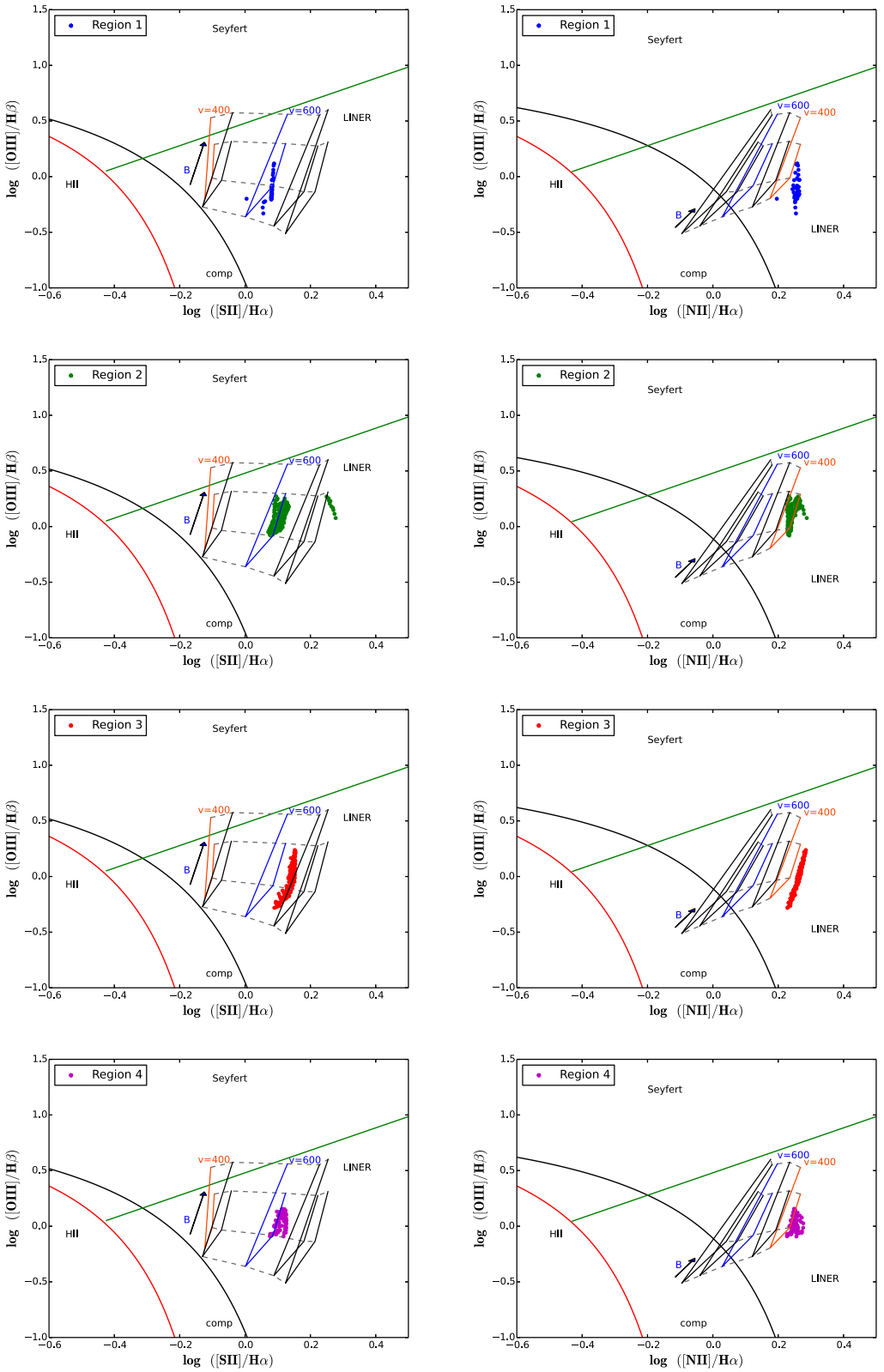

Figure 9. Same as Fig. 8, but for the regions 1–4 selected from the channel maps.

observed inside this small radius. Otherwise, without the presence of an SMBH, the observed rotation curve would follow the one derived from the Sérsic profile. A similar kinematic behaviour as that we found for NGC 5044 has been observed in other early-type galaxies, for example the elliptical M 87 that harbour an SMBH (3×10^9 $M_\odot$, Macchetto et al. 1997; Ho & Kormendy 2000) and the lenticular galaxy NGC 3115 (10^9 $M_\odot$, Kormendy & Ho 2000). Taking the evidences presented here, we conclude that the nuclear

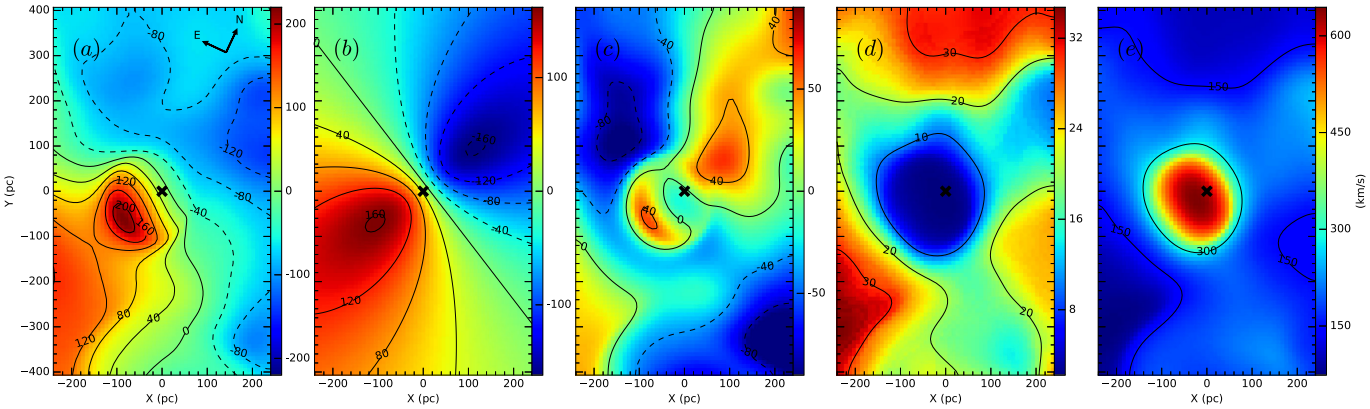

Figure 10. From left to right the panels show (a) the velocity field map with iso-velocities, (b) the best model fitted, (c) the residual map of velocities, (d) the error map of velocity field δ_{v_r} and (e) the velocity dispersion (σ) map. The photometric centre of the galaxy is marked with a symbol 'x' in all maps, and it matches well the kinematic centre (panel b), while the peak of the velocity dispersion is at 30 pc to SE.

Table 4. Gas velocity field parameters.

Parameter	Values
A (km s^{-1})	1285 ± 189
c_0 (pc)	95 ± 5
p	1.5 ± 0.1
v_s (km s^{-1})	2782 ± 1
ψ_0	152° ± 2°
Δx (pc)	0 ± 1
Δy (pc)	18 ± 1

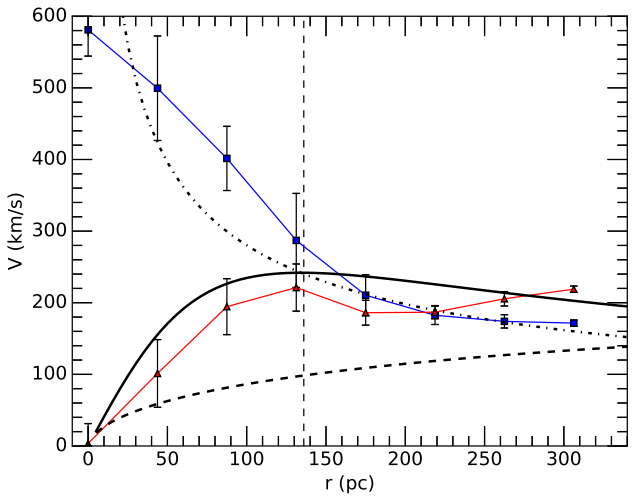

Figure 11. The projected observed rotation curve (red line), overlaid the modelled one (black). The blue line (square points) is the mean velocity dispersion profile along of line of nodes. The dash–dotted line is the BH Keplerian rotation curve. The dashed line is the rotation curve derived from Sérsic's K brightness profile. Note that the gas dynamics on the left side of the vertical line (at 136 pc) is dominated by the BH potential.

gas motions are driven by the gravitational potential of the central SMBH, with mass of $1.8 \pm 1.6 \times 10^9$ M$_\odot$.

7 EVIDENCE OF GAS INFLOW IN NGC 5044

In order to derive the non-rotational velocities, resulting from radial or perpendicular motions, we used the residual velocity map obtained by subtracting the velocity field model from the observed one (Fig. 10c). We can distinguish in the residual map two blueshifted regions with velocities around ~ -40 km s^{-1}, one at east and other at west. Both regions show a peak of -80 km s^{-1}. On the other hand, two redshifted structures are clearly observed along the galaxy's line of nodes (north and south), with velocities of 40 km s^{-1}. These regions have the velocity dispersion of 150 km s^{-1} (see Fig. 10e). The detection of these structures is reliable, because their velocities are higher than the uncertainties (δ_{v_r}) as seen in the velocity field uncertainty map included in Fig. 10 (panel d).

With the purpose of interpreting the structures described above, we used the SHAPE software (Steffen et al. 2010), which allows the user to create interactively 3D spatial structures with their respective velocity fields. The outcome is a projected synthetic velocity field image with a similar orientation to the observer. The output velocities are integrated along the line of sight. We present in Fig. 12 the 3D model for NGC 5044. We assume a rotating disc represented by a cylinder, whose height is one-tenth of the radius and its velocity field is that obtained in Section 6, whereas we assume for all gas filamentary structures a geometry of cone with an aperture of 15°, where the gas inside it has a velocity vector oriented towards the centre. The orientations of the cones and the magnitudes of their respective velocity vectors were constrained requiring that projected velocities of these structure, along the line of sight, match the residual map. We found that the best orientation for the cones is when: (a) the north and south cone filaments are inclined in 20° with respect to the disc and they have a PA with respect to the line of node of 0° and 180°, respectively, and the magnitudes of their respective velocity vectors are 80 km s^{-1}; (b) the cone associated with the east filament is inclined 26° with respect to the disc, has a PA of 90°, and the magnitude of its velocity vector is 105 km s^{-1}; (c) the cone that represents the west filament is inclined in -62° with respect to the disc, has a PA of 270°, and the magnitude of its velocity vector is 105 km s^{-1}. The resulting geometrical configuration, along the line of sight, to represent the gas filamentary structures is shown in Fig. 12(a). The synthetic model of the velocity field is presented in Fig. 12(b). It is created from the sum of the disc and the filamentary structure models, which would represent the observed velocity field as seen in Fig. 10(a). We can see that the model is able to recover the asymmetry in the observed velocity field. In addition, we present in Fig. 12(c) the projected velocities of the cones along the line of sight. It reproduces well the values of residual velocity map (Fig. 10c). This suggests that a suitable interpretation of the residual map could be that the gas in the filamentary structures is

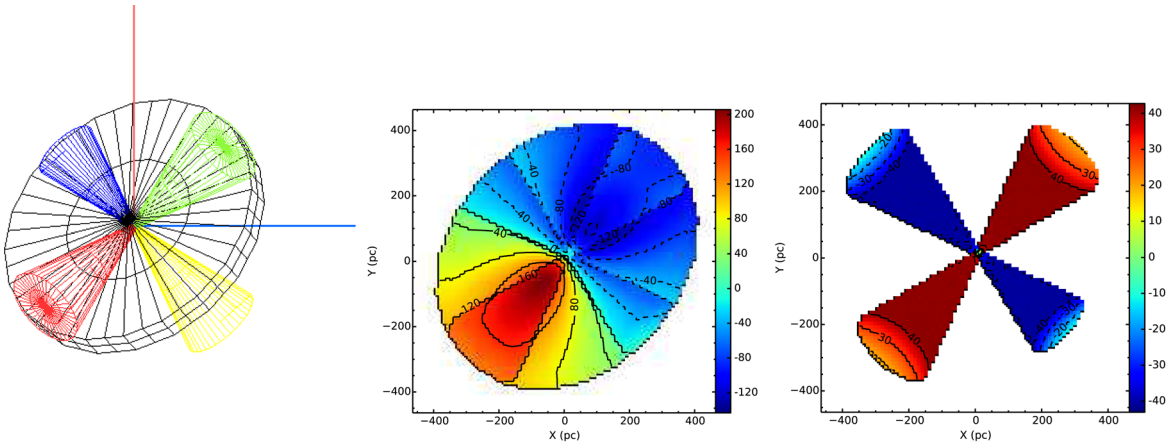

Figure 12. Left-hand panel: representation in 3D to the arrangement of filamentary structures observed from the line of sight. The green cone represents the north filament, the red represents the south one, the blue cone represents the filament at east and the yellow cone represents the filament at west (coming from the far side of the galaxy). Middle panel: the synthetic model of the velocity field along the line of sight. Right-hand panel: the projected velocities of the cones along the line of sight.

falling towards the galaxy centre. This result is in agreement with the findings of David et al. (2014), which suggested that some of the molecular CO clouds they detect are infalling towards the galaxy in a ballistic trajectory. However, we should be caution with our results since they are a simple model approach to reproduce the complex velocity field of the inner 600 pc of NGC5044.

Using the above results we are able to make an estimate of the inflow rate of the gas in the filamentary structure from their observed H α luminosity and the mean magnitude of the velocity of the cone-filaments. Thus, first we integrated the H α flux in all FoV and found $F_{\mathrm{H}\alpha} = 1.65 \times 10^{-12}$ erg cm^{-2} s^{-1}, which at the galaxy distance (Table 1) results in $L_{\mathrm{H}\alpha} = 2.7 \times 10^{41}$ erg s^{-1}. Note that the value obtained here is higher than that found by Macchetto et al. (1996) integrated over the entire galaxy. We attribute this difference to indirect calibration approach used by Macchetto et al. (1996).

The ionized gas mass, $M_{\mathrm{H\,II}}$, can be estimated as follows:

$$M_{\mathrm{H\,II}} = \frac{L_{\mathrm{H}\alpha}}{h\nu_{\mathrm{H}\alpha}} \frac{m_{\mathrm{p}}}{n_{\mathrm{e}}\alpha^{\mathrm{eff}}_{\mathrm{H}\alpha}}, \quad (5)$$

where m_{p} is the proton mass and $\alpha^{\mathrm{eff}}_{\mathrm{H}\alpha}$ is the effective recombination coefficient for H α. Then, by assuming the 'case B' for the recombination (Osterbrock & Ferland 2006), adopting a $T_{\mathrm{e}} = 10\,000$ K and the mean n_{e}= 100 cm^{-3} around of FoV, we found an $M_{\mathrm{H\,II}} = 6.38 \times 10^6$ M$_\odot$. Finally, the inflow rate is calculated with the following expression:

$$\dot{M}_{\mathrm{inflow}} = 4N_{\mathrm{H\,II}}\upsilon A, \quad (6)$$

where $N_{\mathrm{H\,II}}$ is the density of ionized gas, υ is the velocity of the inflowing material, A is the area of the cone base and the factor 4 is due to the number of cones. $N_{\mathrm{H\,II}}$ was estimated adopting a volume of 0.2 kpc^3, which was calculated from the equivalent radius of the physical area of the FoV, $r_{\mathrm{FoV}} = 0.41$ kpc^2. $\upsilon = 93$ km s^{-1} is the mean value of all cones. $A = 0.03$ kpc^2 was calculated from the r_{FoV} and aperture angle of the cones (15°). Then, we found a value of $\dot{M}_{\mathrm{inflow}} \approx 0.4$ M$_\odot$ yr^{-1}. We can now compare it to the mass accretion rate necessary to power the active nucleus by using

$$\dot{M} = L_{\mathrm{bol}}/(\eta c^2), \quad (7)$$

where L_{bol} is the bolometric luminosity, η is the efficiency of conversion of the rest-mass energy of the accreted material into radiation and c is the light speed. We approximated the bolometric luminosity as $L_{\mathrm{bol}} \approx 100 L_{\mathrm{H}\alpha} \approx 2.7 \times 10^{43}$ erg s^{-1} (e.g. Ho 1999; Ho & Peng 2001). We adopted a value of 0.1 for η, which is a typical value for a optically thick and geometrically thin accretion disc (e.g. Frank, King & Raine 2002). Then, we obtain an accretion rate of $\dot{M} \approx 0.005$ M$_\odot$ yr^{-1}. This value is a factor of 10^2 lower than the inflow rate calculated.

One question that rises now is: are these filamentary structures an extension of the larger scale (kpc) filaments earlier studied by Macchetto et al. (1996)? Temi, Brighenti & Mathews (2007) found a remarkably spatial correlation between the filamentary structures in H α and dust detected at 8 and 70 μm. These authors claimed that the dust present in the filaments most likely comes from the galaxy centre. Based on these results, they proposed that NGC 5044 has suffered a recent (10^7 yr ago) feedback where the dust located in the nuclear region was disrupted, heated and transported outward to several kiloparsecs. Pieces of evidence of bubbles were found by Gastaldello et al. (2009) which reported that the inner 10 kpc of this galaxy harbours a pair of cavities together with a set of bright X-ray filaments coincident with H α and dust emission. In addition, Gastaldello et al. (2009) make an estimate of the release time for the bubbles as 1.2×10^7 yr, supporting the scenario proposed by Temi et al. (2007) for this galaxy. Besides our results point to ionized gas flowing towards the galaxy centre, which one can associate with the kpc scale filamentary structure reported for this galaxy. In addition, we found strong evidence for the presence of an accreting SMBH in the nuclear region of NGC 5044, besides a broad component for H α, therefore we speculate that this gas inflow would be originated and transported from large kpc scale to the nucleus of NGC 5044 through the filamentary structures and part of it being accreted by the SMBH and making NCG 5044 active. This would be in agreement with the scenario where the cooling flows into central galaxy of galaxy clusters (which is the case of NGC 5044) are regulated by cyclic feedback episodes (e.g. Peterson & Fabian 2006, and references therein).

8 CONCLUSIONS

We present here, for the first time, high spatial resolution Gemini GMOS/IFU data of the elliptical galaxy NGC 5044 to map the stellar population, emission-line fluxes distribution and gas kinematics

in the inner kpc, with an spatial resolution of 125 pc. Our main conclusions are as follows:

(i) The continuum emission of the inner kpc of NGC 5044 is dominated by an old stellar population. We also detect an intermediate age population (∼40 per cent of an 900 Myr SSP) surrounding the galaxy nucleus. A featureless contribution of ∼20 per cent was found in the galaxy centre, consistent with the detection of a broad component in H α. Besides the maps of mean age and mean Z show a trend consistent with the stellar population becoming more metal poor and younger with increasing distance from the galaxy centre.

(ii) The analysis of the emission-line intensities revels that in the inner kpc of the NGC 5044, the gas distribution is irregular and the H α emission follows the extended filaments. The [N II] and [S II] emission is concentrated in the nuclear region, while the [O III] emission is detected over the whole FoV.

(iii) To fit the central region H α emission lines a broad component is required, with FWHM $\sim$ 3000 km s^{-1} confirming that the FC emission detected in the stellar population fits indeed is due to an LLAGN.

(iv) The FWHM of H α narrow component presents strong variations over the FoV, from FWHM ∼150 km s^{-1} at the outer regions to 1080 km s^{-1} in the galaxy centre.

(v) The dominant excitation mechanism in the filaments is compatible with shock waves with velocity 550 km s^{-1} while in the centre it is explained by an LLAGN. Furthermore, we found that the brighter peak located at east (region 1) and at south (region 3) in the channel maps is co-spatial with the CO emission detected by ALMA.

(vi) From the H α velocity field map, we found evidence of rotating gas. Assuming Keplerian rotation, we estimated a mass of 1.9 $\times$ 10^{9}M$_\odot$ within 136 pc. Besides using $\sigma_\star$ of 279 km s^{-1}and M–σ relation the estimated $M_{\rm bh}$ found is $1.8 \pm 1.6 \times 10^9$ M$_\odot$.

(vii) Filamentary structures, with non-circular motions around |40| km s^{-1}, are revelled in the residual velocity field map, obtained subtracting the disc model from the observed radial velocity field. By using 3D model for these structures, we conclude that the gas inside them is falling towards the nucleus. The inflow rate of 0.4 M$_\odot$ yr^{-1}, was derived from H α luminosity of 2.7 $\times$ 10^{41} erg s^{-1} and with the mean inflow velocity, ∼90 km s^{-1}, estimated for the 3D model. We point out that the inflow rate is 10^2 larger than the accretion rate necessary to power the LLAGN.

ACKNOWLEDGEMENTS

We thank the anonymous referee for his/her careful reading of our manuscript and for his/her insightful comments and suggestions that helped to improve the manuscript. JAHJ thanks to Brazilian institution CNPq for financial support through postdoctoral fellowships (projects 158962/2014-1 and 150237/2017-0). RR thanks to CNPq and FAPERGS for partial financial support to this project. RAR thanks financial support from Brazilian institution CNPq (project 303373/2016-4). TVR acknowledges CNPq for the financial support under the grant 304321/2016-8. Based on observations obtained at the Gemini Observatory, which is operated by the Association of Universities for Research in Astronomy, Inc., under a cooperative agreement with the NSF on behalf of the Gemini partnership: the National Science Foundation (United States), the National Research Council (Canada), CONICYT (Chile), Ministerio de Ciencia, Tecnología e Innovación Productiva (Argentina) and Ministério da Ciência, Tecnologia e Inovação (Brazil).

REFERENCES

Allen M. G, Groves B. A., Dopita M. A., Sutherland R. S., Kewley L. J., 2008, ApJS, 178, 20
Allington-Smith J. et al., 2002, PASP, 114, 892
Annibali F., Bressan A., Rampazzo R., Zeilinger W. W., Danese L., 2007, A&A, 463, 455
Asari N. V., Cid Fernandes R., Stasińska G., Torres-Papaqui J. P., Mateus A., Sodré L., Schoenell W., Gomes J. M., 2007, MNRAS, 381, 263
Belfiore F. et al., 2015, MNRAS, 449, 867
Bertola F., Bettoni D., Dazinger J., Sandler E., Sparke L., 1991, ApJ, 373, 369
Bönsch G., Potulski E., 1998, Metrologia, 35, 133
Bruzual G., Charlot S., 2003, MNRAS, 344, 1000
Caon N., Macchetto D., Pastroriza M., 2000, ApJS, 127, 39
Cardelli J. A., Clayton G. C., Mathis J. S., 1989, ApJ, 345, 245
Cid Fernandes R., Gu Q., Melnick J., Terlevich E., Terlevich R., Kunth D., Rodrigues Lacerda R., Joguet B., 2004, MNRAS, 355, 273
Cid Fernandes R., Mateus A., Sodré L., Stasińska G., Gomes J. M., 2005, MNRAS, 358, 363
Cid Fernandes R. et al., 2009, Rev. Mex. Astron. Astrofis. Ser. Conf., 35, 127
Cid Fernandes R., Stasińska G., Schlickmann M. S., Mateus A., Vale Asari N., Schoenell W., Sodré L., 2010, MNRAS, 403, 1036
Cid Fernandes R., Stasińska G., Mateus A., Vale Asari N., 2011, MNRAS, 413, 1687
Clemens M. S., Bressan A., Nikolic B., Alexander P., Annibali F., Rampazzo R., 2006, MNRAS, 370, 702
Clemens M. S., Bressan A., Nikolic B., Rampazzo R., 2009, MNRAS, 392, L35
Dametto N. Z., Riffel R., Pastoriza M. G., Rodriguez-Ardila A., Hernandez-Jimenez J. A., Carvalho E. A., 2014, MNRAS, 443, 1754
David L. P., Jones C., Forman W., Nulsen P., Vrtilek J., O'Sullivan E., Giacintucci S., Raychaudhury S., 2009, ApJ, 705, 624
David L. P. et al., 2014, ApJ, 792, 94
Davis T. A. et al. 2012, MNRAS, 426, 1574
Davis T. A. et al., 2015, MNRAS, 449, 3503
Dopita M. A., Sutherland R. S., 1995, ApJ, 455, 468
Dopita M. A. et al., 2015, ApJ, 801, 42
Ferland G. J., Netzer H., 1983, ApJ, 264, 105
Ferrari F., Pastoriza M. G., Macchetto F., Caon N., 1999, A&A, 136, 269
Ferrari F., Pastoriza M. G., Macchetto F. D., Bonatto C., Panagia N., Sparks W. B., 2002, A&A, 389, 355
Filippenko A. V., 1982, PASP, 94, 715
Frank J., King A., Raine D. J., 2002, Accretion Power in Astrophysic. Cambridge Univ. Press, Cambridge
Gastaldello F., Buote D. A., Temi P., Brighenti F., Mathews W. G., Ettori S., 2009, ApJ, 693, 43
Gonzalez R. C., Woods R. E., 2002, Digital Image Processing, 2nd edition, Prentice-Hall, Englewood Cliffs, NJ
González-Delgado R. M et al., 2015, A&A, 581, 103
Goudfrooij P., Hansen L., Jorgensen H. E., Norgaard-Nielsen H. U., 1994, A&AS, 105, 341
Halpern J. P., Steiner J. E., 1983, ApJ, 269, 37
Hamuy M., Walker A. R., Suntzeff N. B., Gigoux P., Heathcote S. R., Phillips M. M., 1992, PASP 104, 533
Heckman T. M., 1980, Highlights Astron., 5, 185
Hernandez-Jimenez J. A., Pastoriza M. G., Rodrigues I., Krabbe A. C., Winge C., Bonatto C., 2013, MNRAS, 435, 3342
Hernandez-Jimenez J. A., Pastoriza M. G., Bonatto C., Rodrigues I., Krabbe A. C., Winge C., 2015, MNRAS, 451, 2278
Heyer M. H., Schloerb F. P., 1997, ApJ, 475, 173
Ho L. C., 1999, ApJ, 510, 631
Ho L. C., 2008, ARA&A, 46, 475
Ho L., Kormendy J., 2000, Encyclopedia of Astronomy and Astrophysics. IoP Publishing, Bristol
Ho L. C., Peng C. Y., 2001, ApJ, 555, 650
Hook I. M., 2004, PASP, 116, 425

Kauffmann G. et al., 2003, MNRAS, 346, 1055 (KF03)
Kewley L. J., Heisler C. A., Dopita M. A., 2001, ApJS, 132, 37 (KW01)
Kewley L. J., Groves B., Kauffmann G., Heckman T., 2006, MNRAS, 372, 961 (KW06)
Kormendy J., Ho L., 2000, eaa..bookE2635K
Kormendy J., Ho L. C., 2013, ARA&A, 51, 511
Kurtz M. J., Mink D. J., 1998, PASP, 110, 934
Liu J., 2011, ApJS, 192, 10
Macchetto F., Pastoriza M., Caon N., Giavalisco M., Bender R., Capaccioli M., 1996, A&AS, 120, 463
Macchetto F., Marconi A., Axon D. J., Capetti A., Sparks W., Crane P., 1997, ApJ, 489, 579
Marino A. et al., 2011, MNRAS, 411, 311
Martins L. P., Rodríguez-Ardila A., Diniz S., Riffel R., de Souza R., 2013, MNRAS, 435, 2861
Mateus A., Sodré L., Cid Fernandes R., Stasińska G., Schoenell W., Gomes J. M., 2006, MNRAS, 370, 721
O'Sullivan E., Combes F., Hamer S., Salomé P., Babul A., Raychaudhury S., 2014, A&A, 573, 111
Ogando R. L. C., Maia M. A. G., Pellegrini P. S., da Costa L. N., 2008, AJ, 135, 2424
Osterbrock D. E., de Robertis M. M., 1985, PASP, 97, 1129
Osterbrock D. E., Ferland G. J., 2006, Astrophysics of Gaseous Nebulae and Active Galactic Nuclei, 2nd edn. University Science Books, Mill Valley, CA
Panuzzo P., Rampazzo R., Bressan A., Vega O., Annibali F., Buson L. M., Clemens M. S., Zeilinger W. W., 2011, A&A, 528, A10
Peterson J. R., Fabian A. C., 2006, Phys. Rep., 427, 1
Ricci T. V., Steiner J. E., Menezes R. B., 2014, MNRAS, 440, 2442
Ricci T. V., Steiner J. E., Menezes R. B., 2015, MNRAS, 451, 3728
Rickes M. G., Pastoriza M. G., Bonatto C., 2004, A&A, 419, 449
Riffel R. A., Pastoriza M. G., Rodriguez-Ardila A., Bonatto C., 2009, MNRAS, 400, 273
Riffel R. A., Storchi-Bergmann T., Nagar N. M., 2010, MNRAS, 404, 166
Riffel R., Riffel R. A., Ferrari F., Storchi-Bergmann T., 2011, MNRAS, 416, 493
Sánchez S. F. et al., 2012, A&A 538, 8
Sarzi M. et al., 2010, MNRAS, 402, 2187
Schlafly E. F., Finkbeiner D. P., 2011, ApJ, 737, 103
Singh R. et al., 2013, A&A, 558, 43
Skrutskie M. F., 2006, AJ, 131, 1163
Stasińska G. et al., 2008, MNRAS, 391, 29
Steffen W., Koning N., Wenger S., Morisset C., Magnor M., 2010, IEEE Trans. Vis. Comput. Graphics IEEE Transactions, 17, 454
Steiner J. E., Menezes R. B., Ricci T. V., Oliveira A. S., 2009, MNRAS, 395, 64
Storchi-Bergmann T., Riffel R. A., Riffel R., Diniz M. R., Borges Vale T., McGregor P. J., 2012, ApJ, 755, 87
Strong A. W. et al., 1988, A&A, 207, 1
Temi P., Brighenti F., Mathews W., 2007, ApJ, 666, 222
Thomas D., Maraston C., Bender R., Mendes de Oliveira C., 2005, ApJ, 621, 673
Tody D., 1986, in Crawford D. L., ed., Proc. SPIE Conf. Ser. Vol. 627, Instrumentation in Astronomy VI. SPIE, Bellingham, p. 733
Tody D., 1993, in Hanisch R. J., Brissenden R. J. V., Barnes J., eds, ASP Conf. Ser. Vol. 52, Astronomical Data Analysis Software and Systems II. Astron. Soc. Pac., San Francisco, p. 173
Tran H. D., Tsvetanov Z., Ford H. C., Davies J., Jaffe W., van den Bosch F. C., Rest A., 2001 AJ, 121, 2928
Vega O. et al., 2010, ApJ, 721, 1090
Werner N. et al., 2014, MNRAS, 439, 2291
Yan R., Blanton M. R., 2012, ApJ, 747, 61

This paper has been typeset from a TEX/LATEX file prepared by the author.